



AIAA-2000<sup>1</sup>/~~0~~-0376

*1000-1376-2*

*CP/10/01*

*CP/10/01*

# Large Eddy Simulation Of A Near Sonic Turbulent Jet And Its Radiated Noise

**G.S. Constantinescu & S.K. Lele**

Dept. of Mechanical Engineering &  
Center for Turbulence Research,  
Stanford University,  
Stanford, CA 94305-3030

**39th AIAA Aerospace Sciences  
Meeting & Exhibit  
8-11 January 2001 / Reno, NV**



# LARGE EDDY SIMULATION OF A NEAR SONIC TURBULENT JET AND ITS RADIATED NOISE\*

G. S. Constantinescu<sup>1</sup> and S. K. Lele<sup>2</sup>

Department of Mechanical Engineering and Center for Turbulence Research  
Stanford University, Stanford, CA 94305-3030, USA

## Abstract

In this paper numerical simulations are used to calculate the turbulence dynamics simultaneously with the sound field for a high-speed near-sonic ( $Ma=0.9$ ) compressible jet at two Reynolds numbers of 3,600 and 72,000. LES in conjunction with accurate numerical schemes is used to calculate the unsteady flow and sound in the near field of the jet. It is shown that the jet mean parameters, mean velocity fields and turbulence statistics are in good agreement with experimental data and results from other simulations. The sound in the near-field is calculated directly from the simulations. The calculations are shown to capture the peak in the dilatation and pressure spectra around a Strouhal number  $St=0.25-0.3$ , in agreement with typical jet-noise spectra measured in experiments. Dilatation contours in the near-field show the formation of acoustic waves with a dominant wavelength of 3.2-4 jet diameters, corresponding to the peak in the dilatation spectra. As expected, the non-compact noise sources are found to be most dominant in the region corresponding to the end of the potential core. The contribution of the LES model to the radiated noise appears to be weak and does not contaminate the sound field with spurious high-frequency noise. However, the frequency spectra of the sound show a rapid fall-off away from the peak frequency. This is attributed to the quasi-laminar state of the shear-layers in the region prior to potential core closure, and a possible effect of insufficient azimuthal resolution at the observed location. Further analysis of the effect of the LES model, especially at high frequencies, is needed.

## 1 Introduction

The motivation of this work is to use LES techniques to calculate the acoustic emissions of jet engines. Once the jet simulations are validated in terms of turbulence dynamics, our focus is to predict the radiated jet noise, which is a dominant noise component for most aircraft jet engines at take-off conditions. A study of jet turbulence and its acoustics is relevant for many areas of applications

including mixing enhancement for hot jet-exhaust plumes, but its primary motivation comes from the need to design more efficient engines with reduced noise emissions. Flight tests and wind-tunnel tests are useful but they are expensive, and quantitative measurements of those aspects of turbulence that represent the sources of noise radiation are very difficult, particularly in high-speed flows. This has led to the interest in using computational methods to try to better understand the noise generation. These insights should ultimately allow strategies for controlling or modifying the flow mechanisms to achieve the reduction of the noise emitted by jet engines.

An accurate prediction of the sound radiated by a turbulent jet requires a method capable of reproducing the near-field turbulence dynamics with sufficient fidelity to allow the direct evaluation of the non-compact (distributed) sound sources. Obviously, RANS based methods require too much empirical input and are not suitable to describe accurately the distribution of the acoustic sources in space and time. A great deal of recent understanding of the turbulence physics in high-speed shear flows has come from direct numerical simulations (DNS) at low Reynolds numbers. In fact, Freund<sup>11</sup> has recently conducted DNS of a high-speed jet and its noise. However, as DNS is restricted to Reynolds numbers well below the values of engineering interest, LES techniques appear to be the only realistic available tool to obtain the necessary near-field flow data upon which to base the prediction of sound emitted by propulsive jets. Though still significantly more expensive than RANS methods, LES offers the advantage that little or no empirical input is needed, which is a significant advantage when one is interested in a robust method to predict the radiated sound field. This should allow us to better understand the role of the coherent structures to the noise generation. The fact that the noise spectrum is dominated by the contribution of the large coherent structures justifies the use of LES for noise calculations. However, at very large Reynolds numbers the contribution of the smaller scales to the noise spectrum may be non-negligible in the range of the frequencies of interest, and this problem is yet to be investigated.

\* Copyright ©2001 by the Authors. Published by the American Institute of Aeronautics and Astronautics, Inc., with permission.

<sup>1</sup> Postdoctoral Research Associate

<sup>2</sup> Associate Professor, Member AIAA

Over the last decade LES techniques have advanced to a point where they have been shown to predict complex flows (characterized by a large disparity between the different time and spatial turbulent scales) fairly accurately (e.g., Piomelli<sup>2</sup> and Wang<sup>3</sup>). Use of LES for aeroacoustics applications is a natural development, but one which presents new challenges. The main challenge is related to the large disparity which exists between the energy levels associated with the fluctuations due to the large-scale turbulent motions and those associated with acoustic fluctuations. As most of the acoustic sources are situated in the early part of the turbulent region of the jet, a first requirement is to simulate correctly this turbulent flow so as to be able to calculate accurately the distribution and strength of the acoustic sources. Only the information about the high-frequency turbulence and hence its associated sound is lost in the LES method due to the inherent filtering. Furthermore, no simplifying assumptions about the acoustic wave propagation are required. The only difficulty is numerical; accurate simulation of sound waves concomitantly with the flow structures of the underlying turbulent flow is a considerable task. An important consequence is that accurate prediction of the radiated jet noise using LES techniques requires the use of numerical schemes with low dispersion and dissipation errors. Moreover, the quality of the noise data can be easily compromised by the boundary condition treatment. Higher Reynolds numbers and coarser grids put in turn a higher burden on the robustness and accuracy of the numerical methods used in aeroacoustic simulations. This is why attempts to simulate compressible jets and their radiated noise using LES are quite recent.

Recently the group at NASA Lewis (e.g., Shih et al.<sup>4</sup>) performed a three-dimensional LES calculation of a circular jet at  $Ma=1.4$  in a  $Ma=0.4$  flight stream using a multiblock solver for curvilinear grids. A Kirchhoff method was used to propagate the acoustic emissions to the far-field. Choi et al.<sup>5</sup> simulated a  $Ma=1.2$  jet with coflow at  $Ma=0.2$ , while Zhao et al.<sup>6</sup> have simulated a  $Ma=0.4$  jet at  $Re=5,000$ . The success of most of these simulations was limited to a certain extent by the number of points used. This dictated what scales of fluctuations could be resolved and that in turn limited the frequency content of the simulated noise. Bogey et al.<sup>7</sup> conducted LES of a near sonic jet with a DRP scheme and artificial selective damping of high frequency waves on a Cartesian grid with 6 million mesh points. They used the classical Smagorinsky model to calculate the subgrid (SGS) stresses. To decrease the cost of the computation the grid was refined only in a sector of the computational domain where data was collected in order to calculate the far-field radiated noise. Boersma and Lele<sup>8</sup> performed LES calculations of the near-field of a  $Ma=0.9$  jet using a numerical method very similar to the one used here. The present work is a continuation of their efforts. Finally, it is relevant to mention efforts devoted to develop hybrid schemes which have a cost intermediate to LES and RANS. These schemes, though not as accurate as full LES computations

of the near-field flow, are much less expensive. This approach is being developed at Penn State by Morris and co-workers (e.g., Morris et al.<sup>9,10</sup>) and was applied to calculate circular and rectangular jets at  $Ma=2.1$ . In their method the Navier-Stokes equations were rewritten as equations for the nonlinear perturbations about the RANS solution to the mean flow. This made possible a decomposition of the instantaneous fluctuations into a time-averaged part, a resolved large-scale perturbation and an unresolved small-scale perturbation. The last part was accounted for using a SGS model.

The paper is organized as follows. We start with a description of the numerical method, including the governing equations, implementation of the LES model, flow and boundary conditions, including the treatment of the flow equations at the polar axis. Next, we focus on the jet aerodynamics and we validate our simulations using experimental data obtained for turbulent jets at similar flow conditions. Finally, we use our simulations to investigate the radiated sound in the near-field of these jets. We conclude with a discussion of several issues that we aim to address in future work related to jet noise simulation using LES methods.

## 2 Description of Numerical Method and Flow Conditions

### 2.1 Numerical Method

The primary focus of this paper is on near-sonic compressible cold jets with an acoustic Mach number  $Ma=U_0/c_0=0.9$  and Reynolds numbers  $Re=U_0(2r_0)/\nu=3,600$  and  $72,000$  based on the jet diameter at the inlet ( $2r_0$ ), the jet centerline velocity at the inlet ( $U_0$ ) and the speed of sound at infinity ( $c_0$ ). At this Mach number the turbulent flow was investigated experimentally by Lau et al.<sup>11</sup>, and numerically by Freund<sup>12,13</sup> who performed a DNS simulation at  $Re=3,600$ , by Boersma and Lele<sup>8</sup> who investigated the flow at  $Re=3,600$  and  $36,000$ , and by Bogey et al.<sup>7</sup> who performed LES simulations at  $Re=65,000$ . These near-sonic conditions are motivated by the fan-stream exhaust conditions in a modern turbo-fan engine. Furthermore, due to the relatively high convection speed of the turbulent structures, the total computation time needed to obtain a statistically steady jet is also reduced. Our jet calculations are visualized in figure 1(a)-(b) using snapshots of the vorticity magnitude contours.

The general numerical method is described in Freund et al.<sup>14</sup>, while Boersma and Lele<sup>8</sup> give the details of the implementation of the dynamic LES model in the original DNS code. Following Boersma and Lele<sup>8</sup>, the LES solver uses the non-density weighted compressible filtered variables (no Favre averaging). They found that the non-density weighted filtering as opposed to more widespread Favre filtering improves the robustness of the numerical solution, especially when compact schemes are used. They explained this by observing that the Favre averaged continuity equation is still a non-linear equation that can

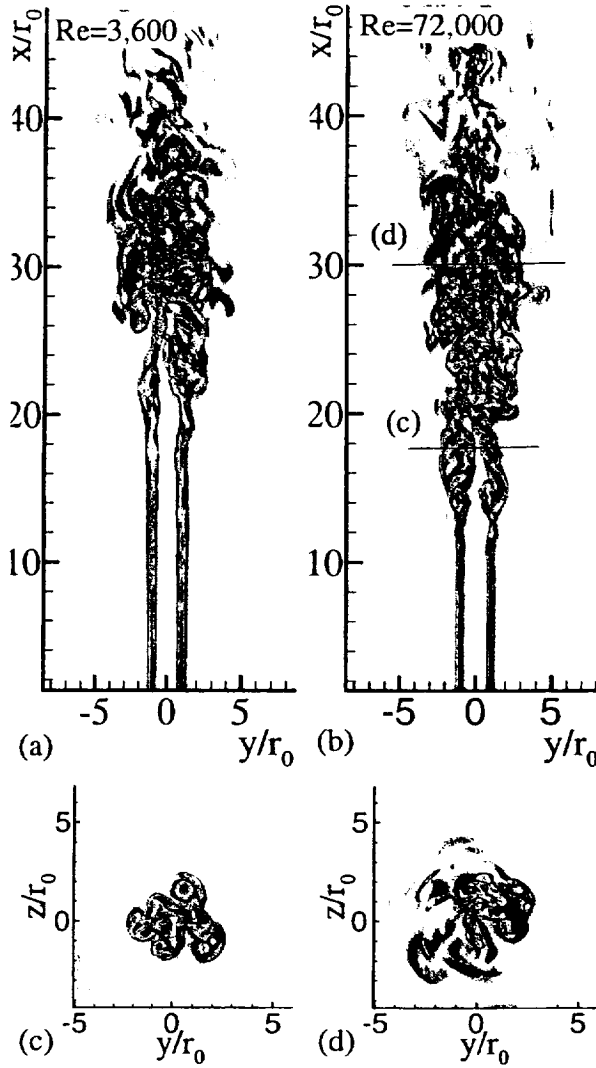


Figure 1: Instantaneous contours of vorticity magnitude. (a)  $Re=3,600$  azimuthal section; (b)  $Re=72,000$  azimuthal section; (c)  $Re=72,000$   $x=17.5r_0$ ; (d)  $Re=72,000$   $x=30.5r_0$

cause numerical instabilities with central-differences schemes. The downside to the non-density weighted filtering is that the form of the filtered equations is slightly more complex. The governing LES filtered equations are (an overbar is used to denote the grid filter):

$$\bar{\rho}_{,i} + (\bar{\rho}\bar{u}_i)_{,i} = -(\overline{\rho u_i} - \bar{\rho}\bar{u}_i)_{,i} \quad (1)$$

$$(\bar{\rho}\bar{u}_i)_{,i} + (\bar{\rho}\bar{u}_i\bar{u}_j)_{,j} = -\bar{p}_{,i} + \bar{\tau}_{ij,j} - (\overline{\rho u_i u_j} - \bar{\rho}\bar{u}_i\bar{u}_j)_{,j} - (\overline{\rho u_i} - \bar{\rho}\bar{u}_i)_{,i} \quad (2)$$

$$(\bar{E})_{,i} + ((\bar{E} + \bar{p})\bar{u}_j)_{,j} = -\bar{q}_{j,j} + (\bar{\tau}_{ij}\bar{u}_i)_{,j} - (\bar{E}u_j - \bar{E}\bar{u}_j + \overline{p u_j} - \bar{p}\bar{u}_j)_{,j} \quad (3)$$

where  $\bar{u}_i$  are the velocity components,  $\bar{p}$  is the pressure,  $\gamma$  is the ratio of specific heats,  $\bar{q}_i = -\kappa\bar{T}_{,i}$  is the conductive heat-flux,  $\bar{\tau}_{ij} = \mu(\bar{u}_{i,j} + \bar{u}_{j,i} - 2/3\delta_{ij}\bar{u}_{k,k}) = 2\mu\bar{S}_{ij}^d$  is the Newtonian stress tensor,  $S_{ij}^d$  is the deviatoric part of the rate of strain tensor,  $E = \bar{p}/(\gamma - 1) + 0.5\bar{\rho}\bar{u}_i\bar{u}_i$  is the resolved total energy density and  $\bar{p}/(\gamma - 1) = \bar{\rho}\bar{T}/\gamma$  is the equation of state. Note a further approximation related to using  $\bar{T}$  rather than the Favre averaged temperature in the equation of state. The filtered continuity equation contains a subgrid mass flux while the filtered momentum equation contains, besides the subgrid momentum flux, an additional term due to subgrid mass flux in the non-density weighted filtering. The presence of the subgrid mass flux in the continuity equation has the effect of improving the robustness properties of the numerical method. In equation (3) we neglected the unsteady term containing the time variation of the subgrid kinetic energy ( $0.5(\overline{\rho u_i u_i} - \bar{\rho}\bar{u}_i\bar{u}_i)$ ) as well as the additional subgrid term originating from filtering of  $\tau_{ij}u_i$ . Using the equation of state and neglecting the convection of the subgrid kinetic energy by the resolved velocity, the last term in (3) representing the subgrid energy flux can be rewritten as  $(\overline{\rho u_i T} - \bar{\rho}\bar{u}_i\bar{T})$ . All these operators are discretized in cylindrical coordinates. The errors introduced by the non-commutativity of the filtering and discrete differentiation operations, as well as the contribution of the trace of the SGS stresses were also ignored.

The code employs a centered six-order compact scheme to evaluate the spatial derivatives in the non-homogeneous directions, and Fourier spectral methods in the homogeneous (azimuthal) direction. The solution is advanced in time using a four-step Runge-Kutta method. These discretization schemes introduce very little artificial dissipation and allow sound waves to propagate accurately with only few grid points per wavelength (Freund and Lele<sup>15</sup>). The number of modes is dropped near the polar axis (this is equivalent to Fourier filtering) so that the CFL constraint will be determined by the radial (or axial) spacing. This avoids the use of a very small time step in our explicit method. The time step is  $\Delta t = 0.01r_0/U_0$ , corresponding approximately to  $CFL=1$ . The computation was carried out on 32 processors of an Origin2000 using message passing interface (MPI).

## 2.2 Subgrid Scale Model

In LES the large, energy-containing scales are computed directly, while the small, unresolved scales that are nearly isotropic and their (non-linear) interaction with the large scales are modeled. However, there is no cut-off between the smaller scales and the larger ones. A lot of progress was made in LES of incompressible flows, particularly of jet flows. However, when applied to compressible flows especially for aeroacoustic applications the effect of the LES model on the flow fields is less understood.

In the present implementation, the LES filtering is implicitly defined by the computational grid used for the large-scale equations. The dynamic procedure is used to calculate the Smagorinsky-like constants in the SGS fluxes in equations (1)-(3). The main idea behind this approach is to determine dimensionless scaling coefficients in SGS models for the filtered nonlinear terms (Pierce<sup>27</sup>). If such a term  $n(a_i)$  is filtered ( $a_i$ 's are the dependent variables), it can be written as the sum of the resolved part and the modeled (subgrid) part:

$$\bar{n}(a_i) = n(\bar{a}_i) + m(a_i) \quad (4)$$

In (4) the grid filter was denoted with an overbar and the filter width is  $\Delta = \sqrt[3]{\Delta_{x_1} \Delta_{x_2} \Delta_{x_3}}$ . A similar relation can be obtained if we apply a second filter, denoted by a hat symbol, and having a width  $\hat{\Delta} = 2\Delta$ :

$$\hat{\bar{n}}(a_i) = n(\hat{\bar{a}}_i) + m(\hat{a}_i) \quad (5)$$

Generally, the subgrid model is written as  $m(a_i) = c s(\bar{a}_i, \Delta)$ , where the 'constant'  $c$  now has a spatio-temporal variation. If we subtract the two previous relations, and allow the 'constant'  $c$  to pass unchanged through the test filtering operator, we obtain an equation in which all terms are computable from the resolved field:

$$\hat{\bar{n}}(\bar{a}_i) - n(\hat{\bar{a}}_i) = c (m(\hat{\bar{a}}_i) - \hat{m}(\bar{a}_i)) \quad (6)$$

The left-hand side in (6) is called the Leonard term (L), while the right hand side is called the model term M. To obtain a single value for  $c$  (L and M are generally non-parallel vectors or tensors), equation (6) is renormalized and solved by least-squares following the procedure developed by Lilly<sup>16</sup>:

$$c = \langle L \cdot M \rangle / \langle M \cdot M \rangle \quad (7)$$

where the square bracket denoted averaging in the homogeneous azimuthal direction. Only the ratio  $\hat{\Delta} / \Delta$  is needed in (7).

Returning to the governing equation system (1)-(3), the subgrid terms in the continuity, momentum and energy equations are modeled according to (6). The dynamic coefficient corresponding to the subgrid mass, momentum and energy fluxes are calculated as follows:

$$c_\rho = -\langle L_i M_i \rangle / \langle M_i M_i \rangle, \quad n_i = \rho u_i, \quad m_i = \Delta^2 |S| p_i \quad (8)$$

$$c_S = \langle L_{ij} M_{ij} \rangle / 2 \langle M_{ij} M_{ij} \rangle \quad (9)$$

$$n_{ij} = \rho u_i u_j, \quad m_{ij} = \rho \Delta^2 |S| S_{ij}^d$$

$$c_E = -\langle L_i M_i \rangle / \langle M_i M_i \rangle \quad (10)$$

$$n_i = \rho u_i T, \quad m_i = \rho \Delta^2 |S| T_i$$

Note that, instead of calculating first the turbulent Prandtl number  $Pr_T$  and then the equivalent 'eddy-viscosity' in the energy equation,  $v_E = c_E \Delta^2 |S| = v_T / Pr_T$ , we calculated  $c_E$  directly. In the previous relations  $|S|$  is the modulus of the strain-rate tensor  $S_{ij}^d$ , and  $v_T$  is the eddy viscosity in the momentum equations. The unsteady term in equation (2) does not require separate modeling; the subgrid mass flux model used in (1) is sufficient.

To maintain stability of the solution field, the resolved flow variables are filtered in all three directions every  $2r_0/c_0$  time units (or every 200 time steps) using an explicit fourth-order accurate filter given by:

$$\bar{f}_i = (-f_{i-2} + 4f_{i-1} + 10f_i + f_{i+1} - f_{i+2}) / 16 \quad (11)$$

A new centerline treatment described in appendix A replaced the old method in which the equations were solved in Cartesian Coordinates. This allowed us to increase substantially (more than 12 times) the time interval at which this filter had to be applied. A detailed discussion of this issue is provided in Constantinescu and Lele<sup>17</sup>. As this filter is applied on the resolved variables, it is important to quantify its effect. In figure 2 the percentage change in the density field is shown. Note that the maximum change relative to the unfiltered density field is around 0.5%, with most of the change at much lower levels, including the area corresponding to the breakup of the potential core. Even though the effect of the damping on the large-scales structures is very low, there is still the possibility that this damping may affect the acoustic waves that originate in the near field. We expect that filtering the resolved variables can be avoided by using finer grids with near-unity aspect ratio cells. In our simulation the aspect ratio is close to 4.0 in most of the physical domain and this is believed to trigger some spurious oscillations. The development of higher-order schemes with behave robustly in treating

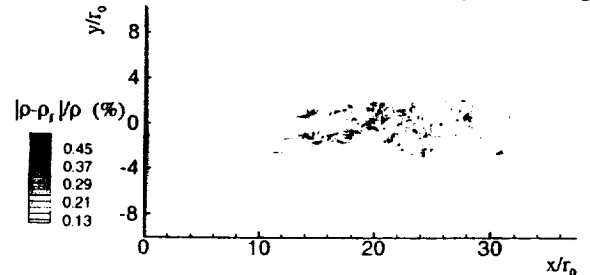


Figure 2: Estimate of error introduced by filtering on the resolved density field

broadband non-linear problems (see, e.g. Nagarajan et al.<sup>28</sup>) will eliminate the need for the introduction of any explicit numerical viscosity in the solution.

The filter defined by (11) is also applied to the rate of strain tensor  $\bar{S}_{ij}$  at every time step before the terms in the SGS stresses are calculated. This is done to avoid the formation of grid-to-grid oscillations in the solution due to under-resolved flow structures. This damping operation is important especially at the higher Reynolds number simulation where practically all the damping comes from the LES term. As noted by Boersma and Lele<sup>8</sup> this filtering affects only the sub-grid terms, and the error associated with it is smaller than the uncertainty involved with the use of the gradient hypothesis to obtain the SGS stresses.

Snapshots of the SGS viscosity fields are displayed in figure 3(a)-(b), corresponding to the two Reynolds numbers. Again the difference in the position of the end of the potential core between the two calculations is obvious. However, if one takes this into account along with the scaling factor equal to the ratio between the two Reynolds numbers, the distribution of the SGS viscosity is very similar. Instantaneous values of the SGS viscosity relative to the molecular viscosity as high as 100 are observed at couple of points in the interior of the jet for  $Re=72,000$ , but 'average' values in these regions are about ten times less.

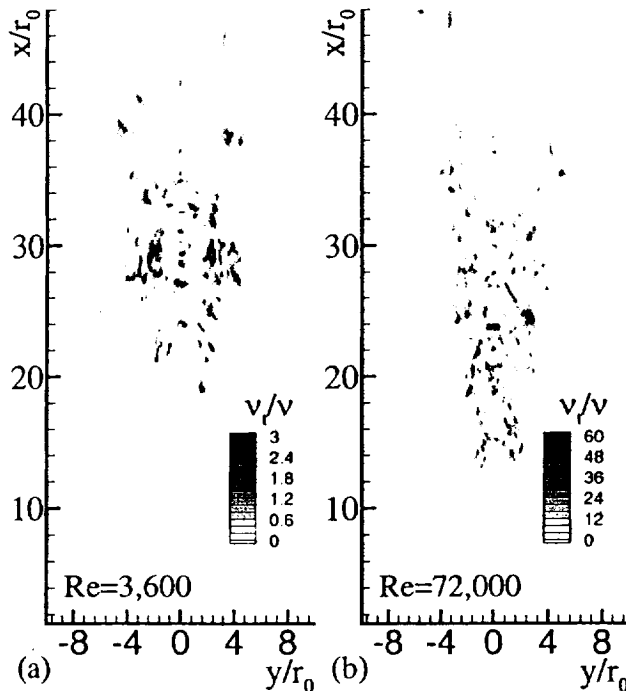


Figure 3: Snapshots of eddy-viscosity fields normalized by molecular viscosity (a)  $Re=3,600$ ; (b)  $Re=72,000$

## 2.3 Inflow Forcing

As the shear layers are already turbulent at this Reynolds number, ideally we would need to have enough points to resolve the turbulence inside these shear layers. This would necessitate a lot of computational points inside the shear layers. The reader is referred to Freund and Lele<sup>15</sup> for an in depth discussion of the issue. Additionally, the presence of the nozzle should be accounted in some way. All these requirements would increase substantially the computer requirements to perform such calculations. Instead, we started with laminar shear layers that were jittered to force transition. This is also evident from the snapshots of the vorticity magnitude shown in figure 1(a) and (b). The mean flow distribution at the inlet plane is assumed to be a rounded top-hat profile with periodic sinusoidal disturbances in the streamwise direction given by:

$$u(r) = U_0 \cdot \left( \frac{1}{2} - \frac{1}{2} \tanh \left( b \cdot \left( \frac{r}{r_0} - \frac{r_0}{r} \right) \right) \right) \cdot (1 + \alpha \cdot \sin(2\pi \cdot St \cdot t)) \quad (12)$$

where the Strouhal number  $St=2r_0f/U_0$  is 0.9, the value of the thickness parameter is  $b=2.8$  (corresponding to a momentum thickness of  $0.09r_0$ ) and the amplitude of the oscillations is  $\alpha=0.005$ . Randomized azimuthal forcing with an amplitude of  $0.025U_0$  and zero mean is applied at the inlet plane to trigger the three-dimensional instabilities and finally transition to turbulence using the following distribution:

$$u_\theta = [0.025U_0 \cdot \exp(-3(1-r/r_0)^2)] \cdot \epsilon \quad (13)$$

where  $\epsilon$  is a random number between  $-0.5$  and  $0.5$ . The exponential function allows the random disturbances to be introduced only in the laminar shear layers. Low amplitude forcing was used because these disturbances do not satisfy the flow equations and generate spurious noise. This can be observed in the lower part of figure 9(a) where waves with wavelength close to  $2r_0$  are originating from the inlet region near the centerline. We could have forced earlier transition, especially at the lower Reynolds number, by increasing the amplitude of the disturbances, but we preferred to keep the spurious noise generated at the jet orifice to a small level.

## 2.4 Boundary Conditions

The computational domain extends to  $X_m=60r_0$  in the streamwise direction and  $R=11r_0$  in the radial direction. The computational grid consists of  $320 \times 192 \times 64$  points in the  $(x,r,\theta)$  directions, or a total of about 3.9 million mesh points, which is about an order of magnitude less than the one used by Freund<sup>12</sup> to calculate a similar jet at  $Re=3,600$  using DNS, but comparable to the meshes used by Boersma and Lele<sup>8</sup> and Bogey et al.<sup>7</sup> in their LES simulations. The points in the radial and streamwise

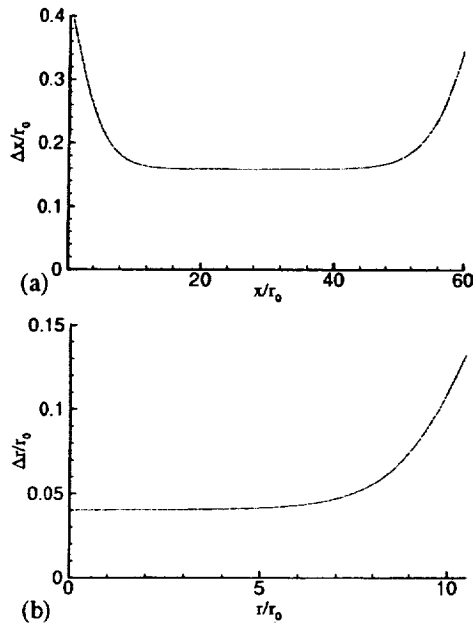


Figure 4: Variation of grid spacing in the computational domain (a) streamwise direction; (b) radial direction

directions are clustered in the region  $r < 5r_0$  and  $10r_0 < x < 40r_0$ , where most of the sound sources are expected to be situated (see also figure 12(a)). In these regions the mesh spacing in the radial and axial directions is approximately  $0.04r_0$  and  $0.16r_0$ , respectively. This mesh should be fine enough to allow an accurate representation of the large-scale structures. Figure 4 displays the distribution of  $\Delta x/r_0$  and  $\Delta r/r_0$  with the streamwise direction. One can see that near the boundaries the mesh spacing increases to  $0.16r_0$  and  $0.40r_0$ , respectively. The number of points in the radial direction corresponding to the initial core region ( $r < r_0$ ) is equal to 25, and the ratio between the initial momentum thickness and the radial grid spacing is 2.2.

The frequency range of the fluctuations which can be captured on this mesh also needs to be kept in mind. Near  $r=0$  the largest mesh spacing is  $\Delta x=0.16r_0$ . A wavelength with twice this spacing gives a Nyquist cut-off Strouhal number  $St_c=6.9$ . However, as the sound waves spread outwards they encounter a mesh with increasing azimuthal spacing. At  $r=8.5r_0$ , a location where much of the acoustic data for the current LES is reported we have  $r\Delta\theta=0.8r_0$  which gives a cut-off Strouhal number  $St_c=1.4$ . Evidently the range  $St > 1.0$  is poorly represented by the azimuthal mesh. This value of the Strouhal number is marked in the figures in which spectral information is presented at  $r=8.5r_0$ .

The formulation of the outflow and to a certain extent of the lateral boundary conditions for aeroacoustic computations is very important. This is because even a small reflection of a large-scale coherent structure exiting the computational domain can dominate the sound field, as

generally the turbulence is several orders of magnitude more energetic than the sound. In the present simulations, zonal boundary conditions with artificial damping are used near the inlet and outlet to absorb outgoing disturbances before they reach the boundary and to avoid spurious noise generation via acoustic reflections at these boundaries. The target solution in these sponge layers was taken to be the self-similar solution of an incompressible jet. Non-reflecting boundary conditions are used at the lateral boundary, as well as damping terms in a layer close to this boundary to avoid the introduction of reflected waves into the domain. The inflow, outflow and lateral sponge layers are  $2.5r_0$ ,  $6.0r_0$ , and  $1.0r_0$  wide, respectively. Taken together they contain roughly 20% of the computational points. The grid in the lateral and outflow sponge layers is stretched and an explicit 6<sup>th</sup> order accurate filter is applied inside these layers every 40 time steps to further damp the near-grid scale turbulence and avoid reflections into the physical domain.

### 3 Results

#### 3.1 Mean Properties and Turbulence Statistics of the Jet

The general structure of the turbulent jet at is highlighted using snapshots of absolute vorticity contours in an azimuthal plane in figures 1(a)- $Re=3,600$  and (b)- $Re=72,000$  and in two plane situated at  $x/r_0=17.5$  and  $30.0$  shown in figures 1(c) and (d) for  $Re=72,000$ . It is observed that vortical structures are generated in the initially laminar shear-layers due to the shear layer forcing. Quasi axisymmetric vortex rings are generated via Kelvin-Helmholtz instabilities as a result of the streamwise forcing of the  $m=0$  mode at the inlet. Three-dimensionality leading to turbulence is accelerated by the interactions of these shear layers. The analysis of the jet mean velocity and turbulence statistics in figures (5)-(6) shows that the transition towards turbulence starts at the end of the potential core situated around  $x=18r_0$  for  $Re=3,600$  and  $x=12r_0$  for  $Re=72,000$ ; the shear layers prior to the end of the 'potential core' in these simulations are quasi-laminar. This has important consequences on the noise produced by this jet. The transition is followed by a region where the turbulence is fully developed and where the mean profiles will be self-similar in the streamwise direction. This region starts at  $x=24r_0$  for the jet at  $Re=3,600$ , and  $x=18r_0$  for the jet at  $Re=72,000$ .

We discuss in detail the distribution of the mean quantities and turbulence statistics for the jet at  $Re=3,600$ , but similar results were obtained for the other case, too. The region in which the jet is self-similar is found to extend up to  $x=40r_0$ , after which the influence of the outflow sponge layer is felt. The statistics were collected over 8,000 time steps, corresponding to  $80r_0/c_0$  time units. Before the statistics were collected, the simulation was run for about 18,000 time steps, corresponding to  $3X_m/c_0$ ; all flow structures associated with the initialization of the

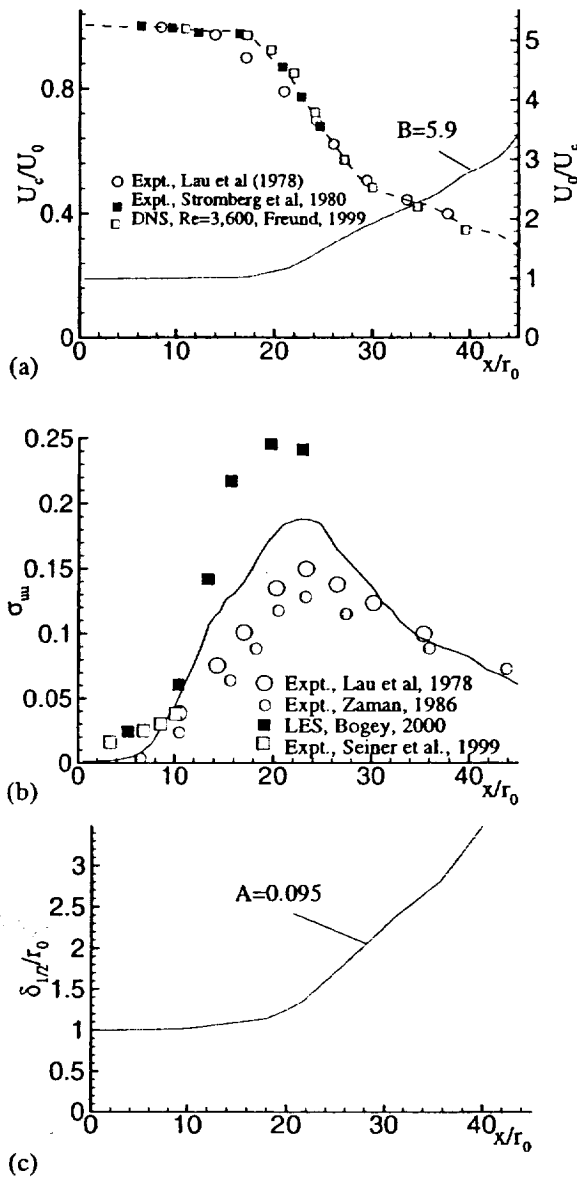


Figure 5: Streamwise evolution of: (a) Mean centerline velocity normalized by the inflow centerline velocity and its inverse; (b) Streamwise turbulent intensity; (c) the half-width of the jet normalized with the jet radius;  $Re=3,600$

simulation had enough time to be convected out of the domain.

In figure 5(a)-(b) we show the distribution of the mean centerline velocity and the longitudinal turbulent intensities as a function of the distance to the jet orifice. Starting at the end of the potential core the centerline velocity decreases and some distance downstream the jet evolves to yield a self-similar jet. As the length of the potential core (core region where the centerline velocity is constant) is different in our simulation from the one

corresponding to the experiment of Stromberg et al.<sup>18</sup> as well as the DNS data of Freund<sup>12</sup> we shifted the data from these experiments/simulations by approximately  $7r_0$ , corresponding to the difference in the length of the potential cores. The data of Lau et al.<sup>11</sup> was not shifted, even though the potential core in their experiments appears to end closer to  $11r_0$ . The differences in the length of the potential cores and hence the position of virtual origin are not due to a problem in our simulation, but rather they are a consequence of the absence of the jet nozzle in the simulations, and the shear-layer state (quasi-laminar). As already mentioned, we avoided the introduction of very strong disturbances in the flow that may have forced earlier transition, as these disturbances are known to radiate sound that will contaminate the sound radiated by the jet itself.

Figure 5(a) clearly shows the decay of the centerline velocity with  $1/x$ , as the inverse of the centerline velocity is seen to grow linearly with  $x$ , starting some short distance after the end of the potential core. One can also infer from the same plot the virtual origin of the jet corresponding to the intersection of that line with  $U_c/U_0=0$ , which is at  $x_0=7.5r_0$ . The decay constant  $B=U_c(x)/U_0 \cdot ((x-x_0)/2r_0)$  is reported to be between 5.4 (Wyganski and Fiedler<sup>11</sup>) and 6.1 (Panchapakesan and Lumley<sup>20</sup>), depending on the experimental setup. A least-square fit through our LES data gives a value for the decay constant  $B=5.9$  which agrees well with the value found in the experiments of Hussein et al.<sup>21</sup> ( $B=5.9$ ), the incompressible DNS simulation of Boersma et al.<sup>23</sup> ( $B=5.9$ ), and the LES simulation of Boersma and Lele<sup>8</sup> ( $B=5.5$ ). In fact, Boersma and Lele<sup>8</sup> suspected that the small length of their domain ( $45r_0$ ) was responsible for the relatively lower value of the decay constant. Same cause may explain the results of Bogey et al.<sup>7</sup> who also found  $B=5.5$  in their simulation. The length of their computational domain was  $30r_0$ , compared with  $60r_0$  in our simulations.

The distribution of the streamwise non-dimensional velocity rms fluctuations  $\sigma_{uu}$  is presented in figure 5(b) along with the experimental data of Lau et al.<sup>11</sup> and Zaman<sup>21</sup>. The overall shape and range of turbulent intensities is correct, but the streamwise fluctuations are overestimated consistently compared to the two sets of experimental data, especially in the earlier part of the jet. The recent PIV data of Seiner et al.<sup>29</sup> is also plotted on the same figure for comparison. Unfortunately, it covers only the initial region of the jet core. We suspect some of the observed differences are due to the way in which transition to turbulence was forced in our simulations, via jittering, compared to their experiment where a nozzle was present. One should mention that Bogey<sup>22</sup> obtained even larger values for the longitudinal fluctuations in the fully developed region, while collecting statistics over a much longer time interval. Their data is also plotted for comparison in figure 5(b). Unfortunately, both Hussein et al.<sup>21</sup> and Panchapakesan and Lumley<sup>20</sup> do not provide this data.

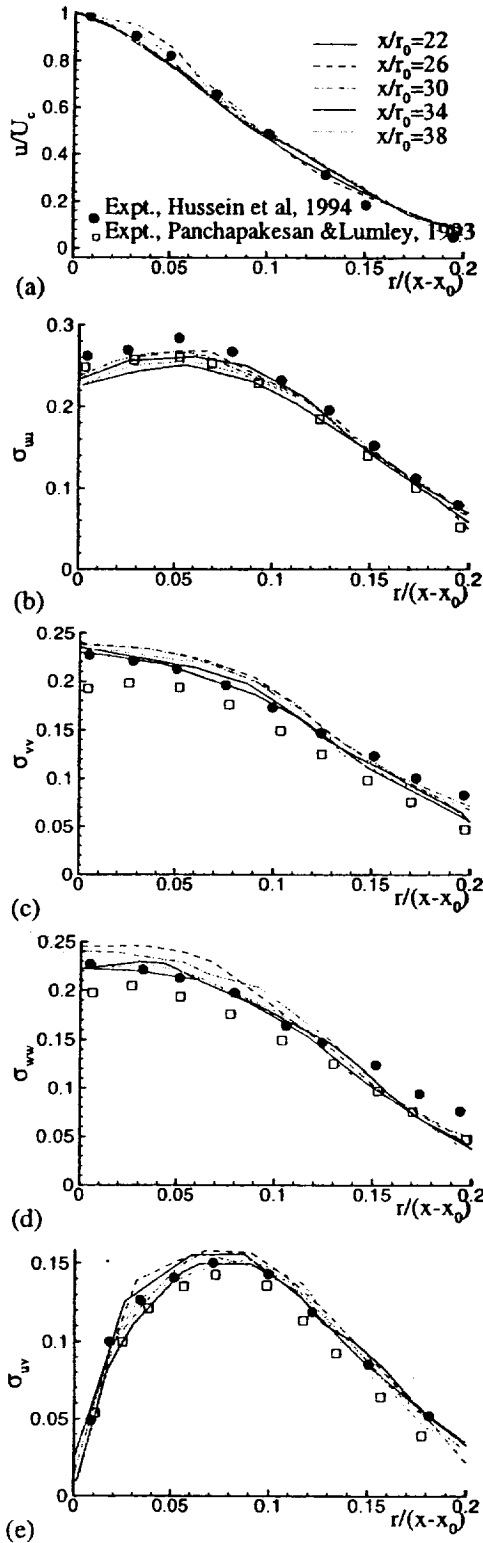


Figure 6: Radial profiles of the Reynolds stresses in the self-similar region of the jet: (a) streamwise fluctuations  $\sigma_{uu}$ ; (b) radial fluctuations  $\sigma_{vr}$ ; (c) azimuthal fluctuations  $\sigma_{vv}$ ; (d) primary shear stress  $\sigma_{uv}$ ;  $Re=3,600$

The growth of the jet is shown in figure 5(c) using the half-width of the jet  $\delta_{1/2}$ , defined as the distance at which the centerline velocity decays by a factor of two, plotted versus the streamwise coordinate. Again, we observe that starting with  $x/r_0=24$  in the fully-turbulent region the jet is growing linearly due to the lateral entrainment of potential flow from the irrotational region, and the slope of this line which defines the spreading rate of the jet is  $A=\delta_{1/2}/(x-x_0)=0.096$ , a value that is close to the one deduced from the experiments of Panchapakesan et al.<sup>20</sup> ( $A=0.096$ ) and Hussein et al.<sup>21</sup> (0.094) and the simulations of Boersma et al.<sup>23</sup> ( $A=0.095$ ) and Bogey et al.<sup>7</sup> ( $A=0.096$ ). The location of the virtual origin deduced from the distribution of the half-width of the jet and the one inferred from the distribution of  $U_c/U_c$  are very close, as expected.

The radial profiles of the mean streamwise velocity,  $u$ , normalized by the centerline velocity,  $U_c$ , are plotted versus the nondimensional radial coordinate  $\eta=r/(x-x_0)$  in figure 6(a) at five stations ( $x/r_0=22, 26, 30, 34, 38$ ) inside the self-similar region. As expected, these profiles are collapsing to a curve that is close to the gaussian velocity profile given by  $U(r)/U_c = \exp(-K(r/(x-x_0))^2)$ , where  $K=\ln 2/A^2=75.2$ . Panchapakesan and Lumley<sup>20</sup> also found  $K=75.2$ , while the simulations of Boersma et al.<sup>23</sup> and Bogey et al.<sup>7</sup> found  $K=76.1$  and  $K=75.2$ , respectively.

The radial profiles of turbulent fluctuations  $\overline{u_x^2}$ ,  $\overline{u_r^2}$ ,  $\overline{u_\theta^2}$  and primary shear stress  $\overline{u_x u_r}$  in the self-similar region are also seen to collapse to curves that agree well with the experimental curve-fits (shown with symbols) obtained by Hussein et al.<sup>21</sup> and Panchapakesan and Lumley<sup>20</sup>. The non-dimensional turbulent intensities in the streamwise ( $\sigma_{uu}$ ) and radial ( $\sigma_{vv}$ ) directions are shown in figure 6(b)-(d) versus  $\eta$ , while the nondimensional shear stress ( $\sigma_{uv}$ ) is shown in figure 6(e). The nondimensionalization of the turbulent rms fluctuations and shear stresses is done using  $\sigma_{u_i u_j} = \sqrt{\overline{|u_i u_j|}}/U_c$ . The agreement appears to be better with the data of Hussein et al. for the streamwise turbulent intensities, while the radial intensities and the shear stress curves appear to be closer to the data of Panchapakesan and Lumley. The fact the agreement is not perfect may be caused by the insufficient radial extent of the computational domain, Reynolds number and Mach number differences between these experiments and our simulations, as well as the effect of the lateral and exit boundary conditions.

Figure 7 shows power spectra of the resolved turbulent kinetic energy (normalized with the kinetic energy at the inflow) in the azimuthal direction at several streamwise locations corresponding to  $x/r_0=10, 17, 24, 30, 37$  for  $r=r_0$ ,  $r=2r_0$  and  $r=3r_0$ , respectively. Except for stations at which the flow is not fully turbulent at that radial location, the form of the spectra shows that the flow is well resolved. It can be observed that the spectra at the stations situated far downstream ( $x/r_0>24$ ) have a slope that approaches  $-5/3$  for the intermediate wavenumbers before

falling off at the high wavenumbers, in agreement with Kolmogorov's theory.

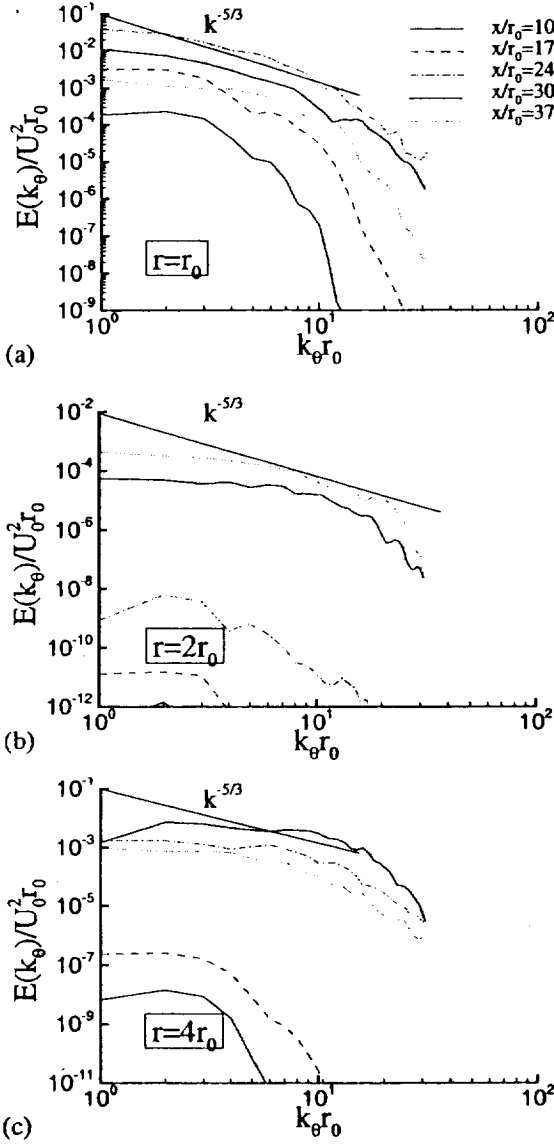


Figure 7: Azimuthal power spectra of the resolved kinetic energy at different streamwise locations for: (a)  $r=r_0$ ; (b)  $r=2r_0$ ; (c)  $r=4r_0$ ;  $Re=3,600$

Finally, it is also of interest to look at the effect of the LES model on the jet turbulence. This is done by comparing at the relative strength of the different terms on the right-hand side of equation (2) for the streamwise velocity component for the  $Re=72,000$  jet where we expect a larger effect of the LES model. In figure 8(a) we plotted the instantaneous fields corresponding to the sum of the convective, pressure and viscous terms, while in figures 8(b) and 8(c) we plotted the contributions from the sub-grid

momentum flux and the time derivative of the subgrid mass flux, respectively. The contour levels go between  $\pm 0.5\rho_0 c_0^2/r_0$  in figure 8(a), between  $\pm 0.01\rho_0 c_0^2/r_0$  in figure 8(b), and between  $\pm 0.001\rho_0 c_0^2/r_0$  in figure 8(c). This shows that the LES contribution via the SGS stresses is far from being dominant. The results at  $Re=3,600$  show a very similar picture in terms of relative magnitude of the LES terms relative to the resolved terms. In conclusion we can say that the agreement of the mean and turbulent properties between the present simulations and the available experimental data is satisfactory. It would be advantageous to compare this LES data with turbulence measurements in a  $Ma=0.9$  jet. We are aware of several groups that are attempting such laboratory experiments, but published data are not available at the present time.

### 3.2 Analysis of Near-Field Acoustic Data

In this section we start using the LES fields as a database for acoustic calculations. A good measure for the sound waves emitted by a flow is the dilatation field. Snapshots of the dilatation fields in an azimuthal plane for both Reynolds numbers are shown in figures 9(a) and (b), while the fields in sections situated at streamwise locations defined by  $x/r_0=23.5, 33, 36.5$  and  $42$  are presented in figures 9(c)-(f), respectively. The presence of the patches of high positive and negative dilatation near the jet center that form a rather regular pattern corresponds to the large-scale vortex rings that are shed at the inlet excitation frequency ( $St=0.9$ ). As these highly coherent structures start to interact, transition to turbulence take place and the distribution of the large scales becomes random. It is in this region that we expect most of the noise to originate.

Away from the region where the noise sources are situated the dilatation is a direct measure of the pressure variation in time, in fact, the linearized (inviscid) energy equation gives:

$$\bar{\nabla} \cdot \bar{\mathbf{u}} = -\frac{1}{\rho_0 c_0^2} p_{,t} \quad (14)$$

We checked relation (14) at points situated away from the region where the non-linear interactions are expected to be important. For instance, the time series corresponding to the RHS and LHS in equation (14) nondimensionalized by  $r_0/c_0$  are shown for a point situated at  $r=8.5r_0$  and  $x=25r_0$ . The two time series are practically identical, when superimposed one on top of the other in figure 10(a). The pressure power spectrum at this point calculated starting from the pressure signal and the dilatation signal (obtained using the equivalent of (14) in Fourier space) are also very similar for the range of resolved frequencies as shown in figure 10(b). The differences are due to low-frequencies variations that are still present in the flow at this region, but it is clear that the dilatation oscillations at this location correspond to sound waves.

With this in mind, one can try to describe qualitatively describe the sound generation using the

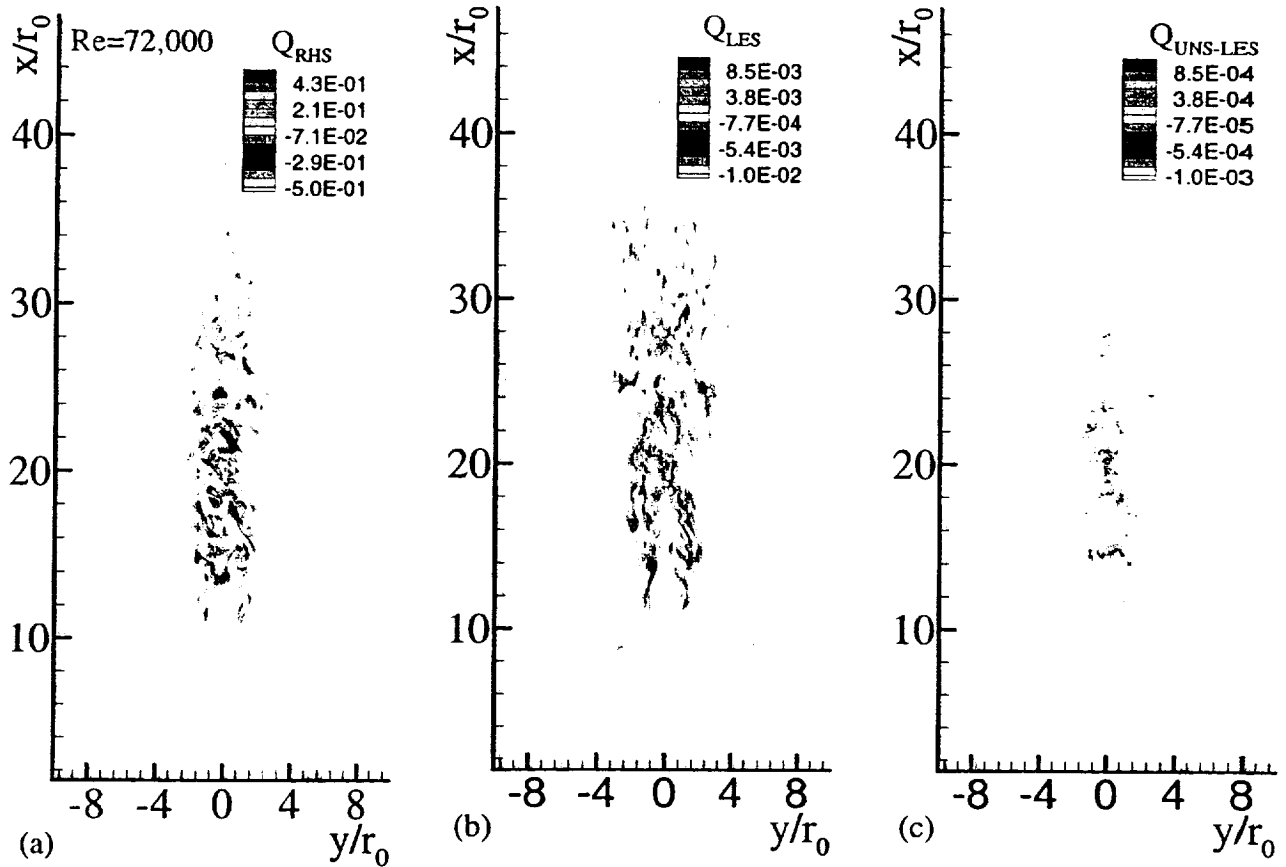


Figure 8: Residual in the streamwise momentum equation for  $Re=72,000$ . Contribution from: (a) resolved terms  $Q_{RHS}$ ; (b) sub-grid momentum flux  $Q_{LES}$ ; (c) sub-grid mass flux  $Q_{UNRES}$

dilatation fields. Figures 9(a) and (b) clearly show dilatation waves with a wavelength of about  $6-8r_0$  that are generated around a virtual origin situated at about  $x/r_0=25$  for the  $Re=3,600$  simulation, and at  $x/r_0=20$  for the  $Re=72,000$  simulation. These locations correspond physically with the termination of the potential core, where most of the noise is expected to originate according to both experimental (Juve et al.<sup>24</sup>) and DNS data (Freund<sup>12</sup>).

As in figure 9(a) the physical domain defined by ( $r>5r_0$ ,  $x>20r_0$ ) appears in to be in the acoustic 'near-field' of the jet, meaning that the dilatation waves visible in the instantaneous dilatation field are traveling as sound waves, it is interesting to look at the time series of dilatation and pressure (figure 11) at a particular location corresponding to point P situated at  $r=8.5r_0$  and  $x=36r_0$  in figure 9(a). Indeed, these time series plotted in figure 11 clearly show the presence of a low-frequency component with a period of about 700 time steps (or  $7.88r_0/c_0$ ) corresponding to  $St=0.26$ . This Strouhal number matches the dominant high wavelength visible in the dilatation field in figure 9(a). On top of the low-frequency waves, oscillations with a higher frequency in the range  $St=1-4$  are also observed. It is not clear if most of these higher frequency fluctuations are spurious. We suspect that these fluctuations can be reduced by running the simulation on a mesh with a

smaller aspect ratio  $\Delta x/\Delta r$  ( $=4.0$  in the present simulations). This is a task for future work. However, physically generated acoustic waves in this frequency range are expected to arise from turbulent shear layers. The presence of dominant low frequency waves at  $St=0.25-0.3$  also explains the dilatation patterns seen in figures 9(d)-(f), where these waves are traveling from the jet center toward the lateral boundary of the physical domain. Note that in these figures we represented the dilatation field over exactly this region that extends only  $10r_0$ , while the wavelength associated with the low frequency wave is around  $7-8r_0$ . This explain why in figure 9(d) and (f) we see only a region of positive dilatation in most of the domain, while the opposite is true in section 9(e) situated in between the previous two. These regions correspond to the compression and rarefaction fronts of the low-frequency wave that is seen in the dilatation time series in figure 11.

In the lower part of figures 9(a) and 9(b) one can see the effect of the disturbances introduced at the jet inlet in terms of sound emissions. Though these disturbances radiate sound at the main excitation frequency (wavelength is close to  $2r_0$ ), they do not contaminate the sound radiated by the jet itself, which seems to be emitted at a much higher wavelength. The other important observation is that the outflow boundary appears to damp the turbulence

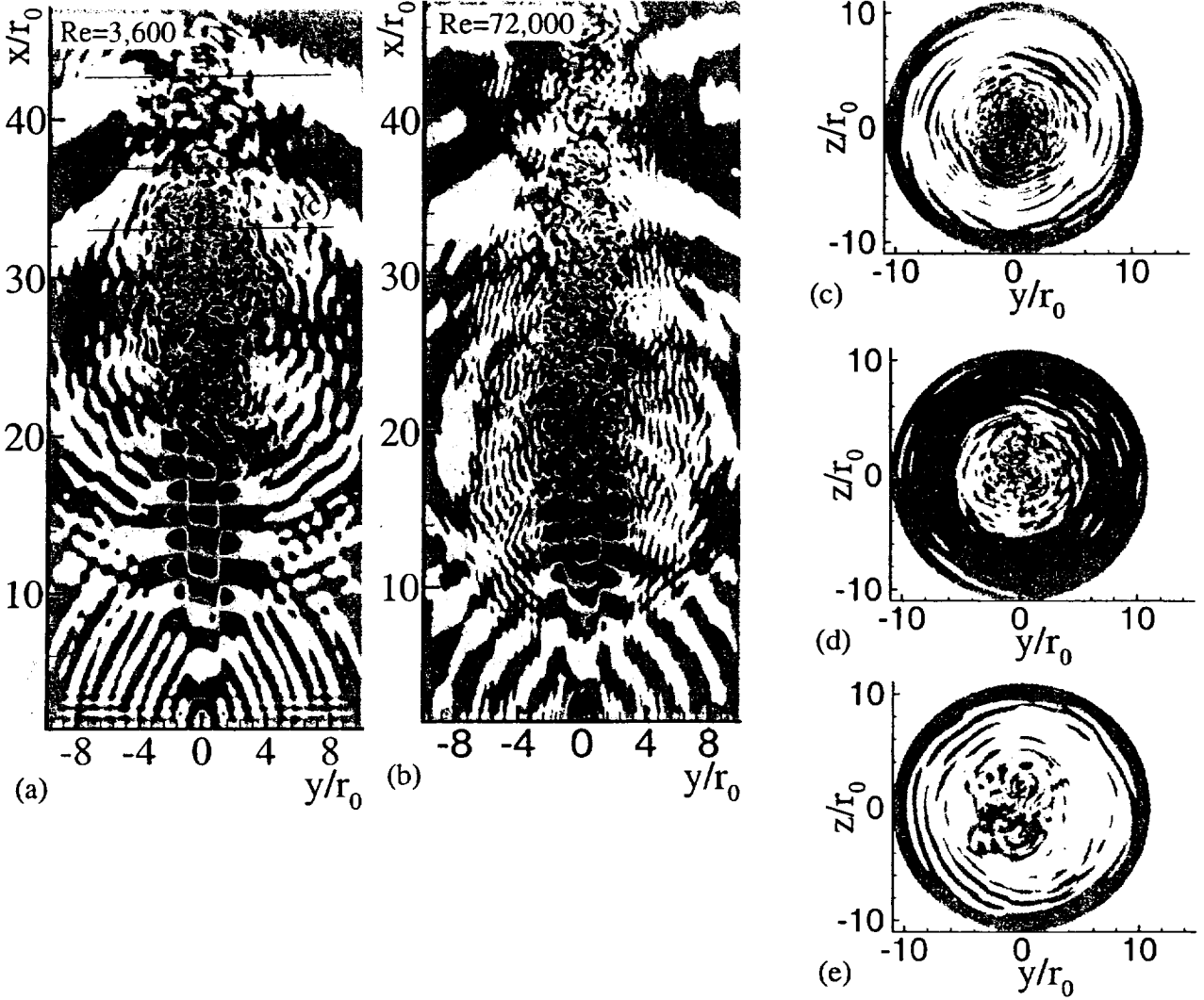


Figure 9: Instantaneous contours of dilatation magnitude, 4 contours equally spaced between  $\pm 0.003c_0/r_0$ . (a)  $Re=3,600$  azimuthal section; (b)  $Re=72,000$  azimuthal section; (c)  $Re=3,600$   $x=23.5r_0$ ; (d)  $Re=3,600$   $x=33r_0$ ; (e)  $Re=3,600$   $x=36.5r_0$ ; (f)  $Re=3,600$   $x=42r_0$

without significant production of spurious sound that will propagate back into the domain and contaminate the sound pattern.

We already alluded to the fact that that as the dominant sound waves originate from a region that corresponds to the termination of the potential core, the 'sound sources' would be expected to be located in the same area. Further evidence for this is given by figure 12(a) where the instantaneous sound sources  $S_{RHS}$  (except the contribution from the LES model denoted  $S_{LES}$ , given in figure 12(b)) are shown for the simulation at  $Re=72,000$ . The acoustic sources are calculated directly from their definitions:

$$S_{RHS} = c_0^2(\overline{\rho u_i u_j} - \overline{\tau_{ij}})_{,i,j} + (\overline{p} - c_0^2 \overline{\rho})_{,i,i} \quad (15)$$

$$S_{LES} = c_0^2(\overline{\rho u_i u_j} - \overline{\rho u_i u_j})_{,i,j}$$

Indeed, for this simulation the instantaneous acoustic sources of relatively high intensity are mostly located in the region  $10r_0 < x < 22r_0$  and  $r < 4r_0$ . Their pattern and overall intensity levels (six equally spaced levels between  $\pm 2.5\rho U_0^2/r_0^2$ ) is quite close to that shown by Freund<sup>12</sup>. Comparison of figures 9(a) and 9(b) also suggests that the LES model does not become acoustically dominant, which is an important concern for application of LES to aeroacoustics. As the levels in figure 9(b) are between  $\pm 0.25\rho U_0^2/r_0^2$  the dominant instantaneous acoustic sources are coming from the resolved-scale terms, while the

contribution of the LES term is at least one order of magnitude lower.

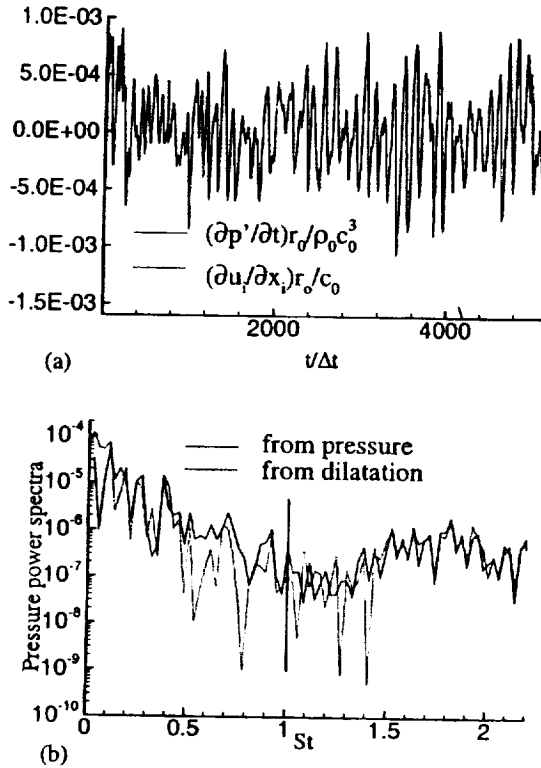


Figure 10: Spectral content of the signal at a point situated at  $(r=8.5r_0, x=25r_0, \theta=0)$  for the  $Re=3,600$  jet (a) Time evolution of the dilatation and pressure time derivative, corresponding to the two terms in equation (14); (b) Pressure power spectra from the pressure and dilatation signals

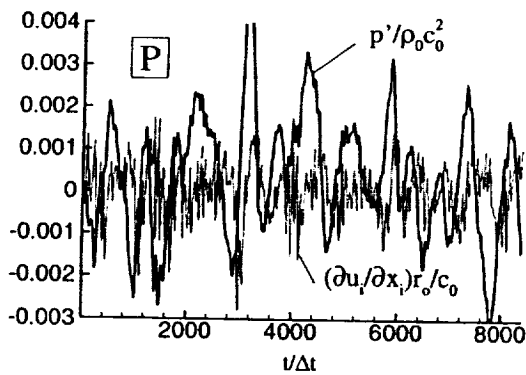


Figure 11: Time evolution of the pressure and dilatation at a point situated in the acoustic 'near-field' at  $(r=8.5r_0, x=36.5r_0, \theta=0)$  for  $Re=3,600$  jet

Figures 13(a)-(c) show power spectra of the dilatation at points situated in the acoustic near field at  $r=8.5r_0$  and  $x=50r_0, 43r_0$  and  $33r_0$ . These locations correspond to points

S1, S2 and S3 in figure 9(a). Their distance from the 'virtual' source center is  $33r_0, 26r_0$  and  $17r_0$  for  $Re=3,600$  and at  $39r_0, 32r_0$  and  $23r_0$  for  $Re=72,000$ . The polar angles are  $15^\circ, 19^\circ$  and  $30^\circ$  for  $Re=3,600$  and  $13^\circ, 15^\circ$  and  $22^\circ$  for  $Re=72,000$ , respectively. The spectra are shown for both simulations, with the data for  $Re=72,000$  being shifted down by a factor of 100 on the vertical axis to allow a better comparison. The noise spectra show that the range of Strouhal numbers corresponding to the peak noise emission is between 0.2 and 0.5, as expected. The power spectra at the higher Reynolds number appear to be more physical in the sense that the second peak at  $St=1-5$  is much weaker and the shape of the spectra is closer to experimental results. Overall, one can observe the fact that for  $Re=3,600$  the peak in these spectra is found around  $St=0.25$  while the spectra at  $Re=72,000$  appear to peak at a slightly higher value of  $St=0.3$ . This is evident if we compare the spectra at points S1 in the  $Re=3,600$  jet and S2 in the  $Re=72,000$  jet that are situated approximately at the same radius from the end of the potential core and have same directivity angle. The second value (given in terms of dominant wavelength  $\lambda=6.6r_0$ ) agrees very well with the value found in the simulation of Bogey et al.<sup>7</sup> at  $Re=68,000$ .

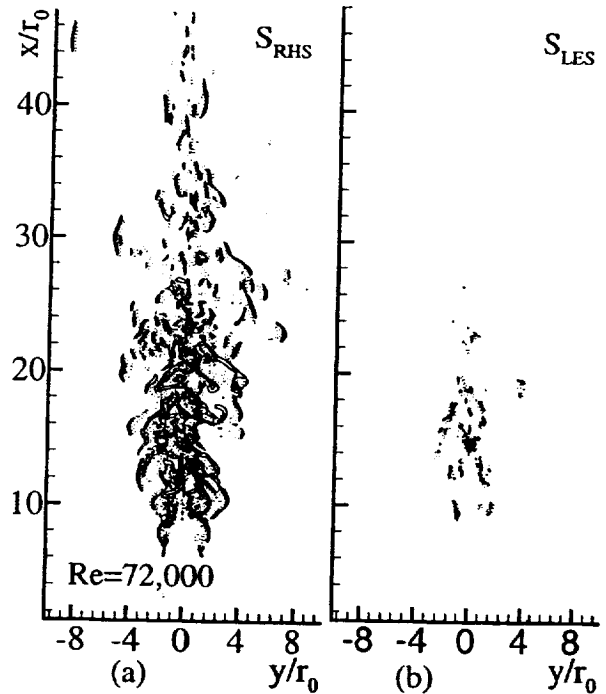


Figure 12: Instantaneous visualization of the Lighthill sound source  $S$  using 6 equally spaced contours between  $\pm 2.5\rho U_0^2 / r_0^2$ . Positive levels are solid, negative levels are dotted. (a) contribution of the resolved variables  $S_{RHS}$ ; (b) LES sub-grid contribution  $S_{LES}$  for  $Re=72,000$  jet

The dilatation contours in the source region sometimes show the formation of a series of wave groups that seem to radiate sound very intensely for a certain period of time. These wave packets with a wavelength smaller than  $2r_0$  seem to form and be destroyed on a relatively short time-scale in a rather random fashion. They appear to be correlated with the relative peak in the noise spectra at  $St > 1$ . However, as the cut-off Strouhal number at locations where the acoustic near-field is measured is close to these values, one probably should discard all together the spectral information for  $St > 1.0$ . This is why a thick line is drawn on our spectra at  $St = 1.0$ .

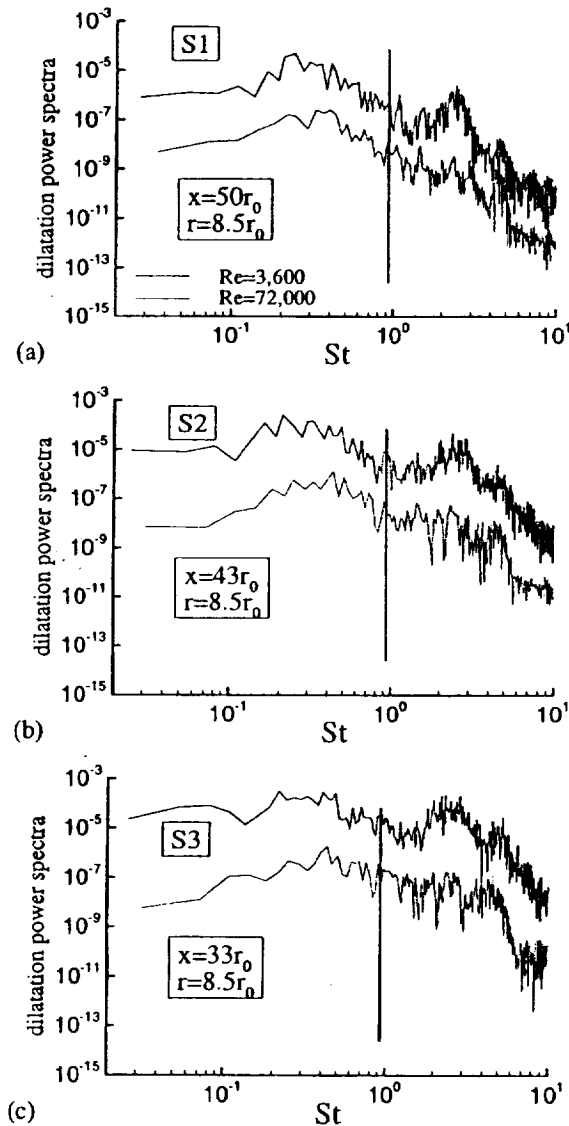


Figure 13: Dilatation power spectra for the simulations at  $Re=3,600$  and  $Re=72,000$  at points (a) S1 ( $r=8.5r_0$ ,  $x=50r_0$ ,  $\theta=0$ ); (b) S2 ( $r=8.5r_0$ ,  $x=43r_0$ ,  $\theta=0$ ); (c) S3 ( $r=8.5r_0$ ,  $x=33r_0$ ,  $\theta=0$ )

Finally, we use the pressure time series at points S1-S3 to calculate the sound pressure levels (SPL) in decibels for the simulation at  $Re=72,000$ . As observed in figure 14, the maximum sound pressure level is obtained around 150-160dB, which is somewhat high but this is expected since the points are situated only  $8.5r_0$  from the jet axis. The overall sound pressure levels (OASPL) for points S1-S3 are 129, 134 and 133dB, respectively. The decay in the SPL between  $St=0.2$  and  $St=1$  is about 28dB (figure 14(b)), which is rather sharp as it translates into a decay of the SPL with frequency following a power law with  $n=4$ , while experimental data suggest  $n=-2.5$  to  $-2$ . However, one may speculate that the decay at higher frequencies is sharp because in our LES simulations we are not capturing the higher frequency sound produced by the turbulent shear layers prior to the potential core closure. Recall that these shear layers were quasi-laminar. There is also some effect of the increasing azimuthal spacing as  $St=1.0$  is approached. Better resolved near-field data is needed to sort out these effects. At the other end of the spectrum our results do not seem to show the very energetic low frequency waves that were present in the computed spectra of Bogey et al.<sup>7</sup>. This may be a consequence of the longer domain and somewhat different treatment of the equations near the outlet boundary that were suspected to be the cause of these waves.

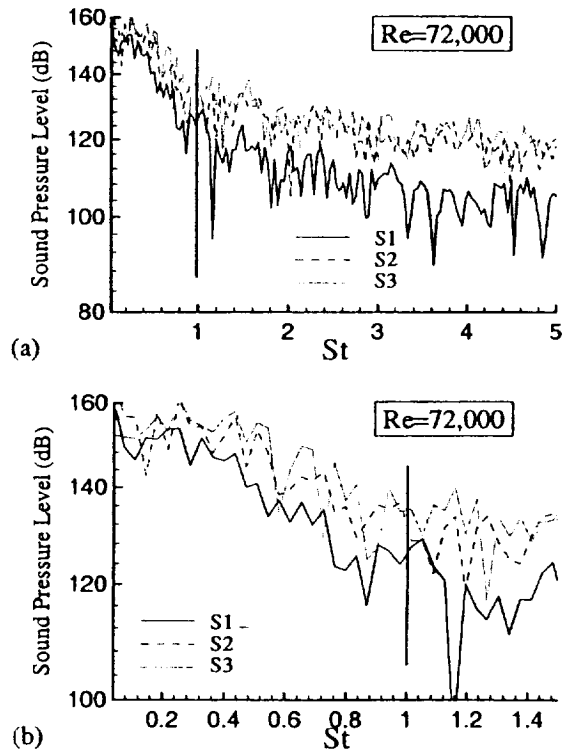


Figure 14: Sound pressure level obtained from the pressure at the points S1, S2 and S3 defined in figure 13 for the simulation at  $Re=72,000$  (a) Strouhal number range between 0.01 and 5.0; (b) detail of the Strouhal number range between 0.01 and 1.5

## 4 Conclusions

In this paper we described the results of numerical simulations of two jets at same Mach number  $Ma=0.9$  but at different Reynolds number of  $Re=3,600$  and  $Re=72,000$  with the aim of showing the feasibility of calculating directly the sound sources and near-field noise using LES. The jet was excited randomly at the inlet plane to force transition. The code uses sixth-order compact schemes to evaluate the derivatives in the radial and streamwise directions while the evaluation of the derivatives in the azimuthal direction is done in the Fourier space. This ensures that a very little amount of artificial dissipation is introduced, allowing the evaluation of the influence of the SGS model separately from the effect of numerical dissipation, as well as making the code suitable to compute directly the radiated noise along with its aerodynamic properties.

The first part of the paper dealt with the description of the jet aerodynamic flow characteristics in terms of the main jet parameters that characterize the growth in the fully developed region, mean profiles, and turbulence statistics. The simulation in terms of aerodynamic data were validated successfully by comparing with available experimental data as well as results of a DNS simulation carried out by Freund<sup>12</sup> at  $Re=3,600$ , as well a recent LES simulation carried out by Bogey et al.<sup>7</sup> at  $Re=68,000$ . Next the noise computed directly in the near-field region corresponding to the physical domain of our simulation was investigated. As expected, the sound sources were found to be situated in the region near the end of the potential core, and the formation of sound waves was captured. The power spectra of these sound waves had its peak around a Strouhal number of 0.25-0.3, in agreement with various experimental studies. A more extensive validation of the sound results is under way. All these results establish that we have a numerical method that allows us to investigate in details the different mechanisms of sound generation.

An ongoing goal of this work is to establish a benchmark LES database for cold jets, that would contain similar calculations at higher Reynolds number (in the range of  $10^6$ ), with the final aim to determine the range of frequencies over which reliable noise data can be extracted from LES and the range of frequencies that would require modeling. We intend to use the near-field data to compute the far-field sound using either a Kirchoff integral method or a wave equation solver. The further development of hybrid methods to calculate the far-field radiated noise starting from direct calculations of the sound in the near-field is essential, especially as more realistic exhaust jet engine configurations are considered.

Our preliminary results suggest that the LES model contribution to the radiated sound is not significant. To address this issue in more details we intend to use the DNS database of Freund<sup>13</sup> to extract space-time correlations of acoustic sources and compare with our LES results) at the same Reynolds number. This would allow to quantitatively estimate the attenuation and suppression of sound, especially at high frequency due to the unrepresented

scales in LES, as well as to investigate in more details the noise contribution of the LES model. We estimate that a more consistent analysis on how the quality of jet-noise predictions depends on the mesh sizes, filtering, etc is necessary to further demonstrate the feasibility of LES methods to aeroacoustics applications.

The question of estimating the higher-frequency sound information that is missing from our simulations because on one hand the LES filtered equations were used, and on the other due to quasi-laminar shear layers, requires further investigation. As pointed out by Freund and Lele<sup>15</sup> predictions methods that allow the acoustic output of the small scales to be estimated and combined with the acoustic output of the resolved scales in LES are highly desirable. We expect that this database will provide valuable help in efforts related to the development of SGS acoustic models that are necessary to account for the noise information lost due to the LES filtering and, in general, the development of LES techniques tailored for noise predictions.

## Acknowledgements

This work was supported in part by Grant No. NA G2-1373 from the NASA Ames Research Center. The original version of the LES code was provided by Prof. B. Boersma. The authors gratefully acknowledge valuable discussions with Prof. J. Freund and Prof. B. Boersma. Computations were run on an Origin 2000 at the ASC MSRC Supercomputing Center.

## References

- <sup>1</sup> Freund, J.B. (2000) "Noise sources in a low Reynolds number turbulent jet at Mach 0.9," submitted to *J. Fluid Mech.*
- <sup>2</sup> Piomelli, U. (1999) "Large-eddy simulation: achievements and challenges," *Progress in Aerospace Sciences*, 35, pp. 335-362.
- <sup>3</sup> Wang, M. (1998) "Computation of trailing-edge noise at low Mach number using LES and acoustic analogy," *Center for Turbulence Research Annual Research Briefs*, 1998.
- <sup>4</sup> Shih, S.H., Hixon, R., Povinelli, L.A. and Mankbadi, R.R. (1998) "Large scale simulation of supersonic jet noise," *AIAA Paper 98-3014*.
- <sup>5</sup> Choi, D., Barber, T.J., Ciappetta, L.M. and Nishimura, M. (1999) "Large eddy simulation of high-Reynolds number jet flows," *AIAA Paper 99-0230*.
- <sup>6</sup> Zhao, W., Frankel, S. and Mongeau, L. (2000) "Large eddy simulation of sound radiation of a subsonic turbulent jet," *AIAA Paper 2000-2078*.

- <sup>7</sup> Bogey, C., Bailly, C. and Juve, D. (2000) "Computations of sound radiated by a 3-D jet using large eddy simulations," *AIAA Paper 2000-2009*.
- <sup>8</sup> Boersma, B.J. and Lele, S.K. (1999) "Large Eddy Simulation of compressible turbulent jets," *Center for Turbulence Research Annual Research Briefs*, 1999.
- <sup>9</sup> Morris, P.J., Long, L.N., Bangalore, A. and Wang, Q. (1997) "A parallel three-dimensional computational aeroacoustics method using nonlinear disturbance equations," *J. Comp. Physics*, **133**, pp. 56-74.
- <sup>10</sup> Morris, P.J., Long, L.N., Wang, Q., Scheidegger, T. and Pilon, A.R. (1998) "High speed jet noise simulations," *AIAA-CEAS Paper 98-2290*.
- <sup>11</sup> Lau, J.C., Morris, P.J. and Fisher, M.J. (1979) "Measurements in subsonic and supersonic free jets using a laser velocimeter," *J. Fluid Mech.*, **93**(1), pp. 1-27.
- <sup>12</sup> Freund, J.B. (1999) "Acoustic sources in a turbulent jet: A Direct Numerical Simulation study," *AIAA Paper 99-1858*, 5<sup>th</sup> AIAA/CEAS Aeroacoustics Conference, 10-12 May 1999, Seattle, WA.
- <sup>13</sup> Freund, J.B. (1999) "Direct numerical simulation of the noise from a Mach 0.9 jet" *ASME Paper FEDSM99-7251*.
- <sup>14</sup> Freund, J.B., Moin, P. and Lele, S.K. (1997) "Compressibility effects in a turbulent annular mixing layer," *Report No. TF-72*, Department of Mechanical Engineering, Stanford University.
- <sup>15</sup> Freund, J.B. and Lele, S.K. (2001) "Computer simulation and prediction of jet noise", to appear in *High Speed jet flows: Fundamental and applications*, Taylor-Francis, 2001.
- <sup>16</sup> Lilly, D.K. (1992) "A proposed modification of the Germano subgrid scale closure method," *Physics of Fluids A*, **3**, pp. 2746-2757.
- <sup>17</sup> Constantinescu, G.S. and Lele, S.K. (2001) "A highly accurate technique for the treatment of flow equations at the polar axis in cylindrical coordinates using series expansions," submitted to *J. Comp. Physics*.
- <sup>18</sup> Stromberg, J.L., McLaughlin, D.K. and Trout, T.R. (1980) "Flow field and acoustic properties of a Mach number 0.9 jet at a low Reynolds number," *J. of Sound and Vib.*, **72**(2), pp. 159-176.
- <sup>19</sup> Wygnanski, I and Fiedler, H. (1969) "Some measurements in the self-preserving jet," *J. Fluid Mech.*, **38**(3), pp. 577-612.
- <sup>20</sup> Panchapakesan, N.R. and Lumley, J.L. (1993) "Turbulence measurements in axisymmetric jets of air and helium. Part I. Air jet," *J. Fluid Mech.*, **246**(1), pp. 197-223.
- <sup>21</sup> Zaman, K.M.Q. (1986) "Flow field and near and far sound field of a subsonic jet," *J. of Sound and Vib.*, **106**(1), pp. 1-16.
- <sup>21</sup> Hussein, H.J., Capp, S.P. and George S.K. (1994) "Velocity measurements in a high-Reynolds-number, momentum -conserving, axisymmetric, turbulent jet," *J. Fluid Mech.*, **258**, pp. 31-75.
- <sup>22</sup> Bogey, C. (2000) "Calcul du bruit aerodinamique et validation de modeles acoustiques hybrides," *Ph.D. Thesis*, Ecole Centrale de Lyon, No. 2000-11.
- <sup>23</sup> Boersma, B.J., Brethouwer, G. and Nieuwstadt, F.T.M. (1998) "A numerical investigation of the effect of the inflow conditions on the self-similar region of a round jet," *AIAA J.*, **10**(4), pp. 899-909.
- <sup>24</sup> Juve, D., Sunyach, M. and Comte-Bellot, G. (1980) "Intermittency of the noise emission in subsonic cold jets," *J. of Sound and Vib.*, **71**(3), pp. 319-332.
- <sup>25</sup> Boyd, J.P. (1989) "Chebyshev and Fourier Spectral methods," Springer-Verlag, Berlin/Heidelberg, 1989.
- <sup>26</sup> Mohseni, K. and Colonius, T. (2000) 'Numerical treatment of polar coordinate singularities,' *J. Comp. Physics*, **157**, pp. 787-795.
- <sup>27</sup> Pierce, C. (2000), Private communication
- <sup>28</sup> Nagarajan, S., Ferziger, J. and Lele, S.K. (2000) "A robust higher-order low-dissipation scheme for large eddy simulation of compressible turbulence," *Bulletin of American Physical Society*, **45**(9), pp. 55.
- <sup>29</sup> Seiner, J.M., Ukeiley, L. and Ponton, M.K. (1999) "Jet noise source measurements using PIV," *AIAA-CEAS Paper 99-1869*.

## Appendix A: Centerline treatment

As the governing system of equations is discretized in cylindrical coordinates, special care is given to the treatment of the equations at the polar axis, due to the presence of singular terms at  $r=0$ . Our experience shows that the quality of the LES solution, especially when compact finite-differences schemes are used, is especially sensitive to the type of equation treatment at the singularity axis.

In the present work we use a new formulation in which a set of exact equations at the singularity axis is

derived using the appropriate series expansions for the variables in the original set of equations. The main idea is to reinterpret the regularity conditions developed in the context of pseudo-spectral methods. Besides increasing considerably the robustness of the numerical method compared to previous versions of the code, an advantage of the proposed treatment is that it preserves the same level of accuracy as for the interior scheme.

The reader is referred to Constantinescu and Lele<sup>17</sup> for a detailed description of the method. Here, we will emphasize only the main points. The governing system of equations (1)-(3) can be written in compact form as:

$$\frac{\partial Q}{\partial t} = \text{RHS}(Q) \quad (\text{A1})$$

where in our case the vector of unknowns is  $Q=(\rho u_r, \rho u_\theta, \rho u_x, \rho, e)$  and the right-hand-side term (RHS) contains the usual operators in cylindrical coordinates associated with the continuity (1), momentum (2) and energy equations (3), including the LES terms. Following Boyd<sup>25</sup>, the most general expansion of a single-valued quantity (S) at the polar axis can be written as:

$$S(r, \theta) = \sum_{m=0}^{\infty} r^m \left( \sum_{n=0}^{\infty} \alpha_{mn} r^{2n} \right) \cdot \cos(m\theta) + \sum_{m=0}^{\infty} r^m \left( \sum_{n=0}^{\infty} \beta_{mn} r^{2n} \right) \cdot \sin(m\theta) \quad (\text{A2})$$

while the expressions for multi-valued quantities (e.g.,  $u_r$  and  $u_\theta$ ) assume the following form:

$$M(r, \theta) = \frac{1}{r} \sum_{n=1}^{\infty} A_{0n} r^{2n} + \sum_{m=1}^{\infty} r^{m-1} \left( \sum_{n=0}^{\infty} A_{mn} r^{2n} \right) \cdot \cos(m\theta) + \sum_{m=1}^{\infty} r^{m-1} \left( \sum_{n=0}^{\infty} B_{mn} r^{2n} \right) \cdot \sin(m\theta) \quad (\text{A3})$$

As any scalar or Cartesian velocity component is uniquely defined at the origin, one can write:

$$\left. \frac{\partial S}{\partial \theta} \right|_{r=0} = 0 \quad (\text{A4})$$

This relation holds, in particular, for  $u_x = u_r \sin(\theta) + u_\theta \cos(\theta)$ , where (y,z) plane is oriented perpendicular to the jet axis. By taking the derivatives with respect to  $\theta$ , and requiring that the relation holds for any  $\theta$ , one obtains:

$$\frac{\partial u_r}{\partial \theta} = u_\theta \quad \text{and} \quad \frac{\partial u_\theta}{\partial \theta} = -u_r \quad \text{at } r=0 \quad (\text{A5})$$

There is another important constraint on the general form of the series expansions for  $u_r$  and  $u_\theta$ . If  $A_{ij}^{(r)}$ ,  $B_{ij}^{(r)}$ ,  $A_{ij}^{(\theta)}$  and  $B_{ij}^{(\theta)}$  are the coefficients of the series expansions for  $u_r$

and  $u_\theta$  in (A3), the following relation holds for all  $i \geq 1$ :

$$A_{i0}^{(\theta)} = B_{i0}^{(r)} \quad \text{and} \quad B_{i0}^{(\theta)} = -A_{i0}^{(r)} \quad (\text{A6})$$

By calculating the derivatives with respect to  $\theta$  and  $r$  of the series expansions given by (A2) and (A3) for all operators present in the RHS of the governing equations (A1) and taking the limit  $r \rightarrow 0$ , a new form of the governing equations that is valid at the polar axis is obtained. These are exact, provided that we can calculate the coefficients  $A_{mn}$ ,  $B_{mn}$ ,  $\alpha_{mn}$ ,  $\beta_{mn}$  for all terms present in the RHS of (A1). However, for a system of PDE's with second-order radial derivatives, as is the case for the Navier-Stokes equations, it is sufficient to calculate at most the coefficients whose indices  $m$  and  $n$  vary between 0 and 2. For instance, the dilatation operator, which is a scalar quantity and should contain only the  $m=0$  mode, can be expressed as:

$$\frac{\partial u_x}{\partial x} + \frac{\partial u_r}{\partial r} + \frac{1}{r} \left( u_r + \frac{\partial u_\theta}{\partial \theta} \right) = \frac{\partial \alpha_{00}^{(x)}}{\partial x} + 2A_{01}^{(r)} \quad (\text{A7})$$

where the streamwise derivative can be calculated with the same method used for points situated away from the polar axis. For a complete description of the form of the RHS expressions corresponding to the fully compressible flow equations including the LES terms, the reader is referred to Constantinescu and Lele<sup>17</sup>.

The last step is to describe how the asymptotic series coefficients that are needed to evaluate the RHS in (A1) are computed. All that is required to calculate these coefficients accurately is to estimate numerically the first and second order radial derivatives of all the variables in RHS with the same order of accuracy as for points away from the polar axis. To do this, the following algorithm is adopted. The computational domain is mapped at every  $x=\text{constant}$ , such that there is no need to specify numerical boundary conditions at  $r=0$ . The mapping function  $(r, \theta) \rightarrow (\hat{r}, \hat{\theta})$  is:

$$\begin{cases} \hat{r} = r, \\ \hat{\theta} = \theta \end{cases} \quad \text{for } \begin{cases} 0 < \theta < \pi \\ 0 < r < R \end{cases} \quad \text{and} \\ \begin{cases} \hat{r} = -r, \\ \hat{\theta} = \theta - \pi \end{cases} \quad \text{for } \begin{cases} \pi < \theta < 2\pi \\ 0 < r < R \end{cases} \quad (\text{A8})$$

The radial derivatives are now taken from  $-R$  to  $R$  with  $r=0$  being a regular interior point instead of a 'numerical' boundary point. This is similar to the method proposed by Mohseni and Colonius<sup>26</sup>, but in their case points in the radial direction were distributed starting with  $r=\Delta r/2$ , instead of  $r=0$ .

Once the values of the variables and of their radial derivatives are known for all  $N_\theta$  directions at  $r=0$  ( $N_\theta$  is the number of points in the azimuthal direction), the relations that define the limit of the series expansions at  $r=0$  for the

variables and their radial derivatives are used to calculate the coefficients in these expansions. For instance, the coefficients  $A_{10}^{(r)}$  and  $B_{10}^{(r)}$  that appear in the expansion of the radial velocity  $u_r$ :

$$u_r = A_{10}^{(r)} \cos(\theta) + B_{10}^{(r)} \sin(\theta) \quad (A9)$$

can be calculated by solving the system of equations that is obtained by writing (A9) at  $\theta$  and  $\theta+\pi/2$ . If  $N_\theta$  is divisible by 8,  $u_r(\theta)$  and  $u_r(\theta+\pi/2)$  corresponds to modes situated  $N_\theta/4$  apart. As these values are known, the calculation of these coefficients is reduced to solving a system of two linear equations with two unknowns. To eliminate the bias toward a certain direction, one can solve the above system for every  $\theta=(2\pi/N_\theta)(n-1)$  with  $n=1$  to  $N_\theta$  and average the results to get final values for  $A_{10}^{(r)}$  and  $B_{10}^{(r)}$ . In a similar way, the coefficients involved in the expressions for the first (and second order derivatives) of  $u_r$  and  $u_\theta$  require solving two (and three) systems of two linear equations. These coefficients serve also to estimate the limit of terms involving the azimuthal derivatives at the polar axis. The coefficients in the expansions are unique so we do not have to choose any arbitrary directions as was the case when the equations were solved in Cartesian coordinates at the singularity axis.

